Published as: Nardi T., Sangermano M., Leterrier Y., Allia P., Tiberto P., Månson J.-A.E, UV-Cured Transparent Magnetic Polymer Nanocomposites, Polymer, 54, 4472-4479 (2013). DOI 10.1016/j.polymer.2013. 06.052. © 2013. This manuscript version is made available under the CC-BY-NC-ND 4.0 license http://creativecommons.org/licenses/by-nc-nd/4.0/

UV-CURED TRANSPARENT MAGNETIC POLYMER NANOCOMPOSITES

Tommaso Nardi[*], *Marco Sangermano*[$], *Yves Leterrier*[*ø], *Paolo Allia*[$], *Paola Tiberto*[#] *and Jan-Anders Månson*[*]

[*]*Laboratoire de Technologie des Composites et Polymeres*

Ecole Polytechnique Federale de Lausanne

[$]*Politecnico di Torino, DISAT, Corso Duca degli Abruzzi 24, 10129 Torino (Italy)*

[#]*INRIM, Electromagnetism, Strada delle Cacce 91, 10135 Torino (Italy)*

(ø) corresponding author yves.leterrier@epfl.ch

Abstract

Magnetite nanoparticles are synthesized by thermal decomposition of $Fe(acac)_3$ and subsequently coated with a silica shell exploiting a water-in-oil synthetic procedure. The as- produced nanopowder is mixed with a photocurable hyperbranched resin and the polymerization process is studied by means of real-time FTIR (RT-FTIR). Owing to the presence of the silica shell, the photocuring ability of the systems containing core-shell structures is highly improved compared with that of the formulations filled with bare magnetite nanoparticles, allowing the efficient polymerization of a 100 μm-thick film loaded with an unprecedented 8 vol% of magnetic filler.

1. Introduction

Polymer nanocomposites have drawn much attention in the last years due to the synergistic combination of advantages deriving from their organic and inorganic constituents. The exploitation of the intrinsic properties of the polymeric matrix (flexibility, ductility etc.) and the nanofiller (hardness, electrical, magnetic and optical properties) makes them appealing candidates for many applications such as coatings, inks and specialty plastics [1-5]. In particular, magnetic nanocomposites could broaden their applicability range to magnetic sensors and actuators[6], catalysis[7], magnetic shape memory polymers [8] and electromagnetic shielding[9].

Among the various curing processes, UV-triggered radical polymerization represents an economic, fast and non-toxic method [10], especially for coatings. Many papers deal with the good photocurability of polymeric systems containing non-pigmented nanoparticles, such as SiO_2. The high particles content of these nanocomposites does not strongly preclude good polymerization kinetics and can often lead to advantageous changes in properties such as Young's modulus[11], Vickers hardness[4], refractive index[12], polymerization shrinkage[13] and viscosity[14].

On the contrary, the photopolymerization process of magnetic nanoparticulate systems is highly hindered by the presence of pigmented particles, which reduce the light accessibility of the photoinitiator thus strongly inhibiting the radical formation process[15]. For this reason, a major drawback of photocurable polymeric composites containing magnetic nanoparticles is represented by the maximum particle volume content (a few vol%[6]) that can be achieved while preserving satisfactory polymerization rate and final conversion. In other words, high contents of magnetic particles can be attained only at the cost of drastically decreasing the composite film

thickness[6]. As a matter of fact, UV curing of magnetic nanocomposites is limited to very thin films or low particle contents.

In this paper, we compare two different nanocomposites based on the same hyperbranched acrylated polymeric matrix (HBP): one containing bare Fe_3O_4 nanoparticles (NPs) whereas the other loaded with Fe_3O_4@silica core-shell nanoparticles. We highlight that, for equal concentrations, a much faster and complete curing process takes place when core-shell nanostructures are employed, paving the way to the inclusion of much higher particle volume contents compared to those attainable employing bare nanoparticles. Moreover, due to the high filler concentration, the as-formed nanocomposites show remarkable magnetic properties, although the silica shell may have a slight detrimental effect on the magnitude of the magnetic response.

2. Experimental

2.1 Materials

Iron (III) acetyacetonate ($Fe(acac)_3$, 99+%) and benzyl ether (99%) were purchased from Acros. Oleylamine (Tech.70%), polyoxyethylene(5)nonylphenyl ether, branched (Igepal CO-520) and ethanol (≥99.5 %) were purchased from Aldrich. Cyclohexane (p.A.) was purchased from Applichem. Ammonia solution (25% min) and tetraethyl orthosilicate (TEOS, ≥99%) were purchased from VWR and Merck, respectively. The hyperbranched polyester acrylated oligomer (characterized by a functionality of 16, a density of 1.13 g cm^{-3} and a glass transition temperature in cured state of 165 °C) was purchased from Sartomer (commercial name CN2302). The photo-initiator (2,4,6-trimethylbenzoyldiphenyl phosphine oxide) was purchased from BASF (commercial

name Lucirin TPO). All products were used as received without any further purification.

2.2 Synthesis of Fe_3O_4 nanoparticles

To synthesize Fe_3O_4 nanoparticles, the procedure reported by Xu et al.[16] was followed with minor modifications. In a typical synthesis of ~6 nm Fe_3O_4 NPs, $Fe(acac)_3$ (6 mmol) was dissolved in 30 mL of benzyl ether and 30 mL of oleylamine. After having been dehydrated at 110 °C for 1 h under N_2 atmosphere, the solution was heated to 260 °C and aged at this temperature for 1 h. The resulting black solution was then allowed to cool down to room temperature, and 100 mL of ethanol were added to precipitate the nanocrystals. Nanoparticles were hence separated by centrifugation and dispersed in cyclohexane.

2.3 Synthesis of Fe_3O_4@silica core-shell nanoparticles

In a typical synthesis of ~25 nm Fe_3O_4@silica NPs, 3 ml of the solution of oleylamine-coated Fe_3O_4 NPs in cyclohexane (~15 mg/ml) were added to 420 ml of cyclohexane and mixed with 21 ml of Igepal CO-520. The pH was adjusted to ~10 through the addition of ammonium hydroxide (25%) and the formation of a transparent brown microemulsion was ensured with the aid of a sonicator. Then, 1.2 ml of TEOS were added and the reaction was stirred at room temperature for 48 h. Subsequently, the reaction mixture was washed with ethanol and particles underwent different cycles of centrifugation and redispersion to remove the surfactant. Finally, nanoparticles were dried under vacuum.

2.4 Preparation of polymer-magnetite nanocomposites

First, the photo-initiator (6 wt%) was dissolved in the HBP at 65 °C and stirred for 15 min. The selected amount of Fe_3O_4 suspension in cyclohexane was then added to the HBP and the mixture was stirred for one hour at room temperature. The solvent was evaporated under vacuum until no more weight variation of the suspension was detected. Nanocomposites containing core-shell nanoparticles were prepared mixing a certain amount of dried Fe_3O_4@silica NPs in the HBP and promoting their dispersion with the addition of a small amount of hexane. The mixture was then stirred for one hour at room temperature and sonicated for another hour. The solvent was hence evaporated under vacuum until no more weight variation of the suspension was detected. The effective nanoparticles content of the different formulations was calculated starting from the weight residual as from TGA experiments and converting it to particle volume % through the densities of the various components.

2.5 NPs and nano-composites characterization

The morphology of the magnetic nanoparticles and the silica-coated magnetic nanoparticles were characterized using a Philips/FEI CM12 microscope at an accelerating voltage of 120 kV. Typically, few drops of nanoparticles diluted suspensions (in cyclohexane for Fe_3O_4 NPs, in ethanol for Fe_3O_4@silica NPs) were deposited on carbon filmed copper grids (200 mesh, Plano GmbH).

To analyze the solid UV-cured films, 80 nm-thick slices were cut at room temperature using a Leica microtome and a Diatome Cryo 45° diamond knife and deposited on carbon filmed copper grids (200 mesh, Plano GmbH).

The curing process was investigated by Real-Time FT-IR analysis (RT-FTIR). The formulations were coated onto a silicon wafer by using a wire-wound applicator (film

thickness of 100 μm). A medium pressure mercury lamp (Hamamatsu LC-8) equipped with an optical waveguide was used to induce the photopolymerization at room temperature (UVA intensity on the surface of the sample around 20 $mW \cdot cm^{-2}$).

Acrylic double bond conversion as a function of irradiation time was investigated using a Thermo-Nicolet 5700 instrument and samples were exposed simultaneously to UV light and to the IR beam. Acrylic double bond conversion was followed by monitoring the decrease in the absorbance of the C=C double bond centered at 1610 cm^{-1}. The signal decrease was normalized with the carbonyl peak centered at 1760 cm^{-1} and the percent conversion (α) of C=C bond was calculated by the equation (1) [17]

$$\alpha(\%) = \frac{(A_{C=C} / A_{C=O})_{t_0} - (A_{C=C} / A_{C=O})_t}{(A_{C=C} / A_{C=O})_{t_0}} \times 100 \quad (1)$$

where $(A_{C=C} / A_{C=O})_{t_0}$ and $(A_{C=C} / A_{C=O})_t$ are the relative absorbance of C=C bonds before curing and at a given curing time *t*, respectively.

UV-vis analyses were performed using a JASCO V-670 in the spectral range between 200 and 800 nm. The formulations were coated onto a quartz wafer by using a wire-wound applicator to maintain a film thickness of 50 μm.

Determination of the crystalline phase of the iron oxide nanoparticles was done by means of a X-ray diffraction analysis using a PANalytical MPD Pro diffractometer with Cu K_α radiation source (1.54 Å).

Thermo Gravimetric Analysis (TGA) was performed with a Mettler TGA/DSC under air at a constant heating rate of 10 °C/min.

Magnetization loops of bare Fe_3O_4 NPs and of Fe_3O_4@silica core-shell NPs in powder form were measured at T = 100 K, 200 K and 295 K by means of a Vibrating

Sample magnetometer (VSM) operating in the ±15 kOe field range and equipped a liquid-N_2 continuous-flow cryostat. Magnetization loops of photo-cured nanocomposites containing 0,7% of bare NPs and 8% of core-shell NPs were measured at room temperature by means of a sensitive Alternating-Gradient Field Magnetometer (AGFM) operating in the ±15 kOe field range.

3. Results and Discussion

3.1 Fe_3O_4 nanoparticles

The transmission electron microscopy (TEM) image of Fe_3O_4 NPs is shown in Figure 1a. From the corresponding histogram (Figure 1b), it can be seen that the size distribution is quite narrow and characterized by a Gaussian bell centered at 5.65±0.13 nm.

Figure 1: TEM micrograph of Fe_3O_4 nanoparticles (a) and corresponding particle size distribution (b)

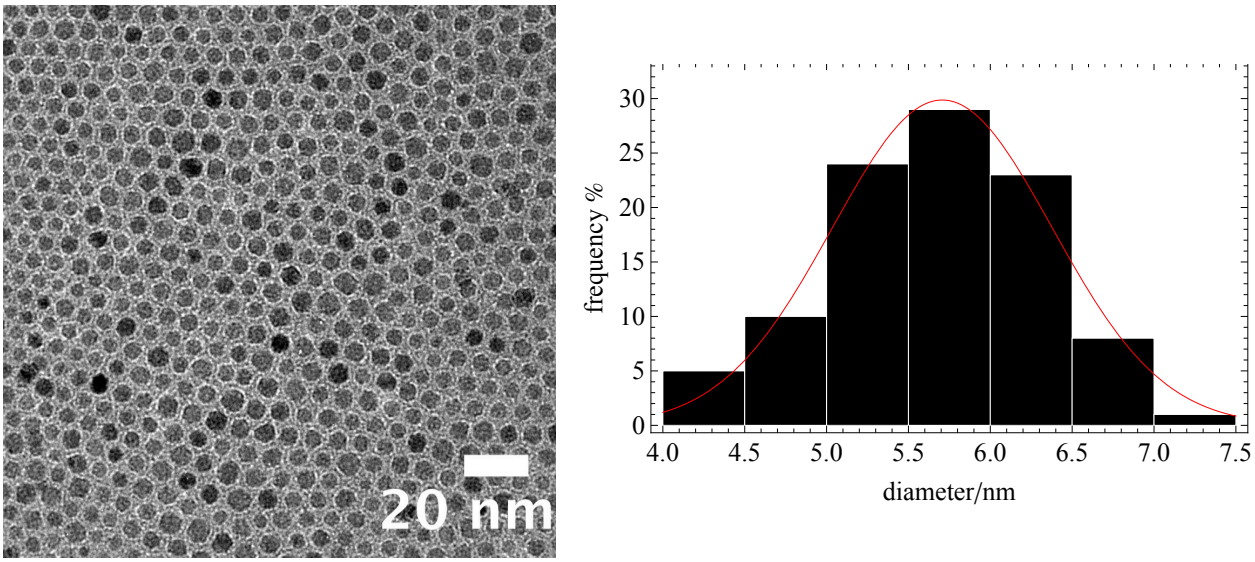

X-ray diffraction (XRD) was used to determine the crystallographic features. As can be seen from Figure 2, the intensity and the position of the recorded peaks match well with the standard magnetite. From the width at half maximum (FWHM) of the observed peaks, it was possible to calculate the mean crystallite size (L) through the Scherrer equation[18]:

$$B(2\theta) = \frac{k\lambda}{L\cos\theta} \tag{2}$$

where k (Scherrer constant) was assumed to be 0.9, λ is the radiation wavelength (0.154 nm), B is the full width at half maximum (in radians) and θ is the Bragg angle. The calculated mean crystallite size resulted to be ≈ 6 nm, in very good agreement with the value obtained by TEM analyses (5.65 nm).

Figure 2: XRD pattern of Fe_3O_4 nanoparticles (a) and the standard Fe_3O_4 diffraction peaks (b)[19].

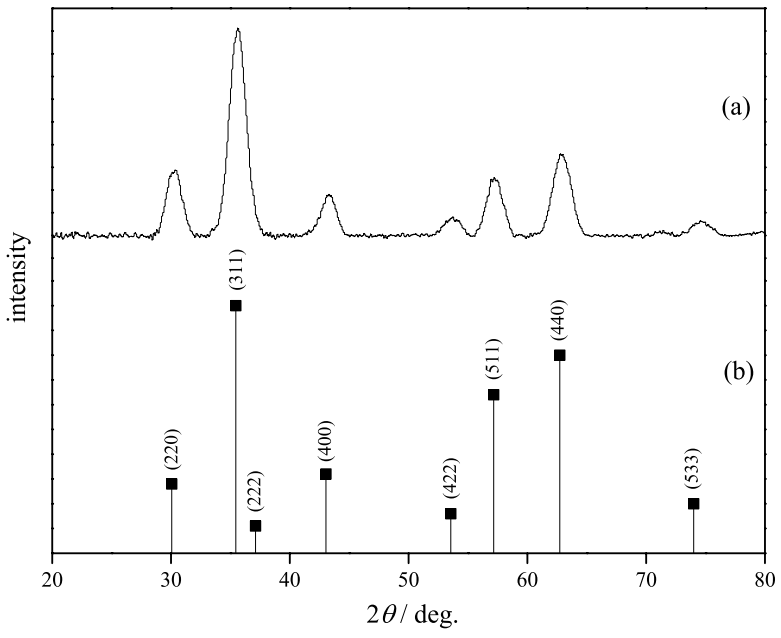

Isothermal magnetization curves of bare Fe_3O_4 NPs measured at three different temperatures are reported in Fig. 3 (left panel). All curves are characterized by the absence of magnetic hysteresis and by a clearly non-saturating behavior at high fields. High field magnetization values of 32, 31, 27 emu/g are observed at T = 100, 200, 295 K, respectively. These are fairly good values, even if much lower than the saturation magnetization of bulk magnetite (92 emu/g at room temperature [20]). On the other hand, it is a well known fact that the saturation magnetization can be notably reduced in magnetite nanoparticles with respect to bulk specimens [21]because of the prominent role played by magnetic disorder entailed by surface magnetic anisotropy. The experimental curves can be easily fitted to Langevin functions; this feature along with the absence of measurable hysteresis should point to a nearly perfect superparamagnetic (SP) behaviour of bare NPs; however, this is not the case, because the scaling law predicted for SP nanoparticles is not followed, as clearly shown in Fig. 3 (right panel) where M/Ms is plotted as a function of the ratio H/T[22]. Ms was estimated by extrapolating the experimental curves for $H \rightarrow \infty$ using an approach-to-saturation law of the type $M(H) = M_s - \square/H$.

Figure 3: (left panel) magnetization curves of bare magnetite NPs at three different temperatures; (right panel) plot of reduced magnetization M/M_s as a function of H/T

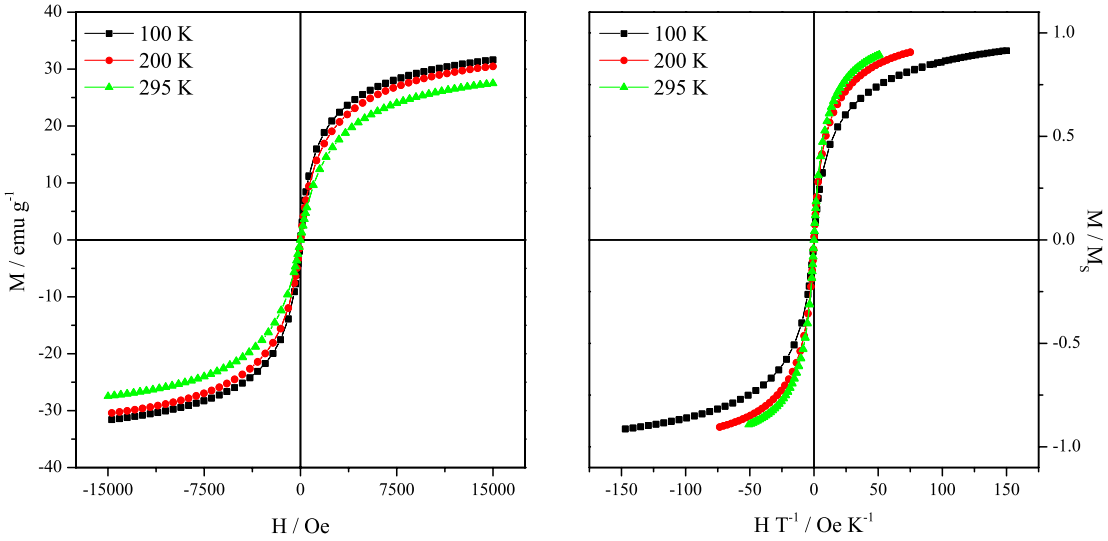

3.2 Fe_3O_4@silica nanoparticles

TEM analyses on Fe_3O_4@silica core@shell nanoparticles evidenced a log-normal particle size distribution with a mean diameter of 25.61±1.58 nm (Figure 4a-b). The morphology of the as-produced nanoparticles was more irregular than that of bare magnetite and in many cases more than one core was included within the same silica shell.

Figure 4: TEM micrograph of Fe_3O_4@silica nanoparticles (a) and corresponding particle size distribution (b)

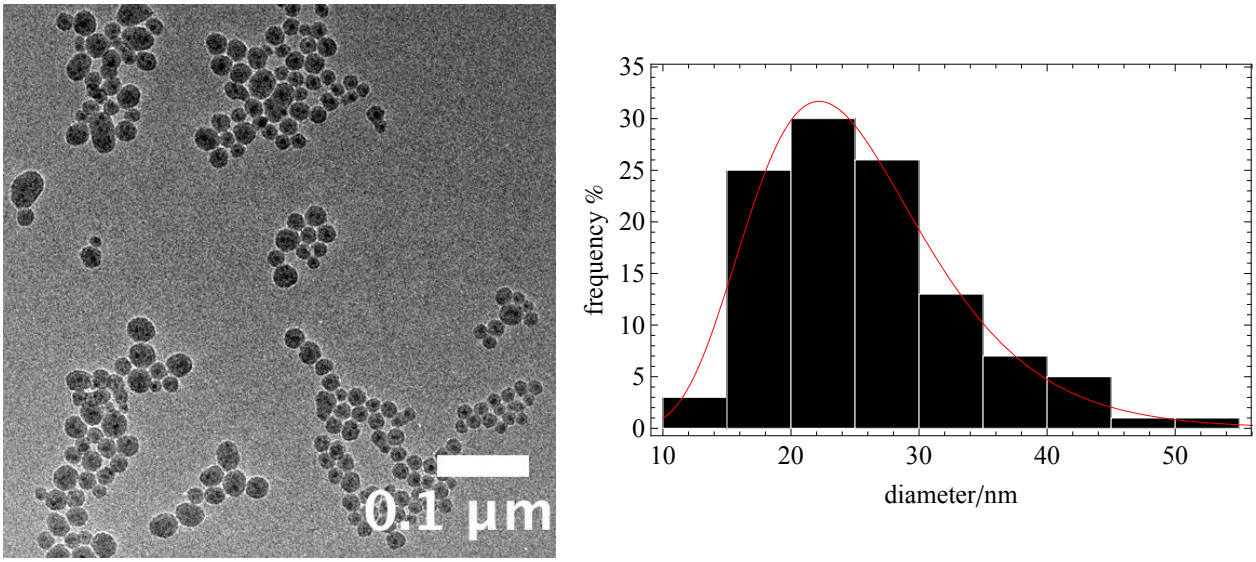

Isothermal magnetization curves of Fe_3O_4@silica core-shell NPs measured at three different temperatures are reported in Fig. 5 (left panel). The curves exhibit a general behavior similar tp bare NPs (i.e., a non-saturating trend at high fields together with no detectable hysteresis loop); the high-field magnetization per unit mass of the sample is very low in this case, being equal to 3.8, 4.0, 4.2 emu/g at T = 100, 200, 205 K, respectively. However, the magnetization value markedly increases when it is estimated considering the mass of iron oxide alone. Judging from TEM images, the typical number of magnetite NPs enclosed in a single silica shell is between 3 and 4. For an average occupancy of 3 iron oxide NPs per each silica shell, a room-temperature high-field magnetization value of 38 emu/g is estimated from Fig. 5; for an occupancy of 4 NPs, the estimate decreases to 29 emu/g; both values are comparable with the result for bare NPs, indicating that enclosure in the silica shell can have only minor effects on the intrinsic magnetization of our magnetite NPs. Even in this case, the experimental curves can be easily fitted to Langevin functions;

the SP scaling law is much better followed than for bare NPs, although not yet perfectly (right panel of Fig. 5). This can indicate a reduced interaction with respect to bare nanoparticles; however, further magnetic measurements, including lower temperature loops and FC/ZFC magnetic susceptibility curves [23] are needed to ascertain the real nature of the magnetic response of both bare and core-shell NPs.

Figure 5: (left panel) magnetization curves of core-shell magnetite NPs at three different temperatures; (right panel) plot of reduced magnetization as a function of H/T

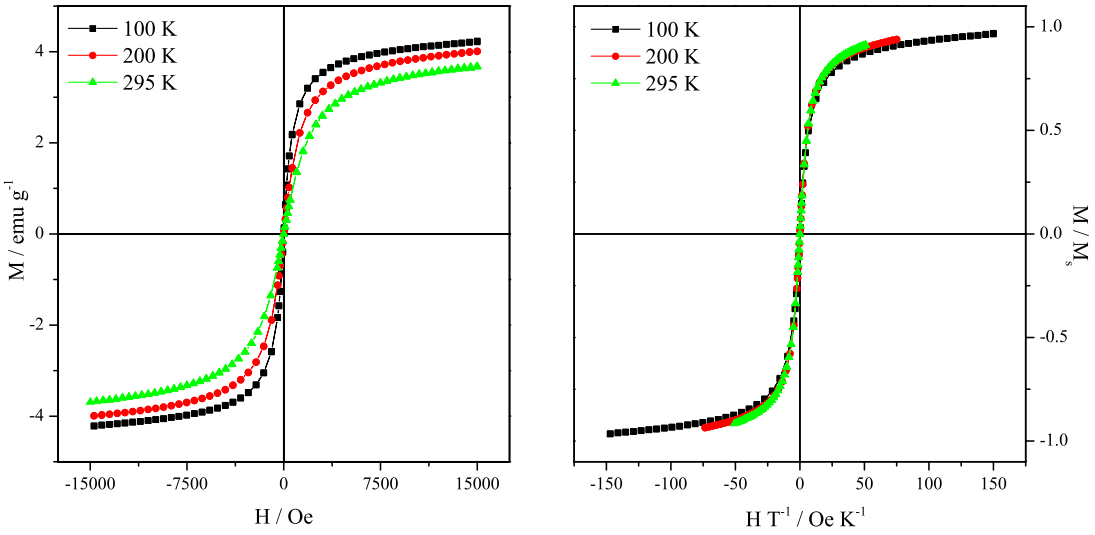

3.3 Photopolymerization process

The synthesized magnetic nanoparticles (Fe_3O_4 or Fe_3O_4@SiO_2 NPs) were dispersed into the acrylated HBP as a reference resin. The effect of the presence of the filler on the UV-curing process was evaluated by FT-IR following the acrylic double bond conversion as a function of the irradiation time. While the plateau value gives the final acrylic double bond conversion, the slope of the curve gives an indication of the polymerization rate.

In Figure 6 the conversion curves as a function of irradiation time are reported for the pristine HBP resin and for the same resin containing either Fe_3O_4 bare or Fe_3O_4@SiO_2 NPs. The final acrylic double bond conversion values are reported in Table 1.

Figure 6: Conversion curves as a function of irradiation time for the pristine HBP resin (●) and for the formulations containing 0.7 vol% Fe_3O_4 (■), 1 vol% Fe_3O_4 (♦), 4 vol% Fe_3O_4@SiO_2 (▲) and 8 vol% Fe_3O_4@SiO_2 (▼)

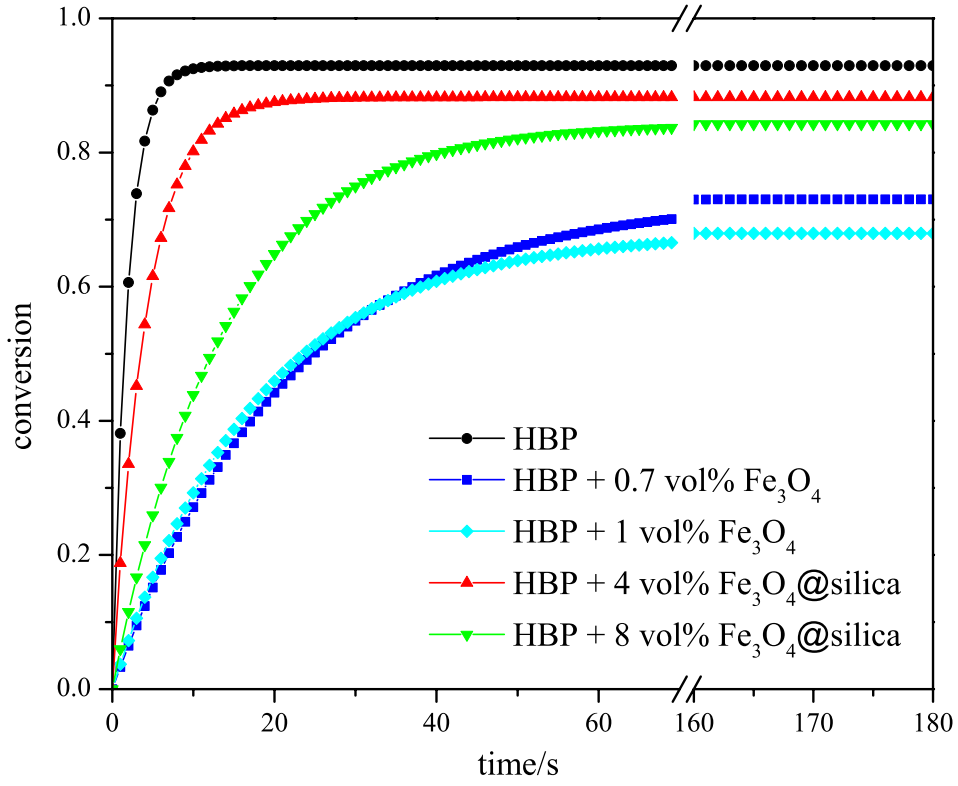

Table 1: Final acrylic double bond conversion evaluated by the plateau reached in the RT-FTIR analyses.

ϕ (vol %)	**α_{max} % (HBP + Fe_3O_4)**	**α_{max} % (HBP + Fe_3O_4@silica)**
0	0.93	0.93
0.1	0.89	0.90
0.7	0.73	0.89
1	0.68	not tested
2	0.58	not tested
4	too opaque to cure	0.88
8	too opaque to cure	0.84
12	too opaque to cure	0.63

The pristine acrylic resin shows a quite good reactivity towards the UV-induced radical chain-grow polymerization, reaching an almost acrylic double bond complete conversion after few seconds of irradiation.

The addition of the Fe_3O_4 NPs induced a severe reduction of both 7the filler was added in the photocurable resin, the final conversion decreased from 93% to 73%. When 2 vol% of the filler was added, the final conversion reached only 58%. It was not possible to further increase the magnetite NPs since above 2 vol% the photopolymerization was hindered and a sticky film was obtained.

The decrease of acrylic double bond conversion by increasing the Fe_3O_4 NPs content can be explained through a competitive absorption between the photoinitiator and the inorganic particles in the UV region between 200 and 400 nm (Figure 7).

Figure 7: UV-vis spectra of polymeric nanocomposites containing different quantities of bare Fe_3O_4 NPs (a) and core-shell Fe_3O_4@silica NPs (b)

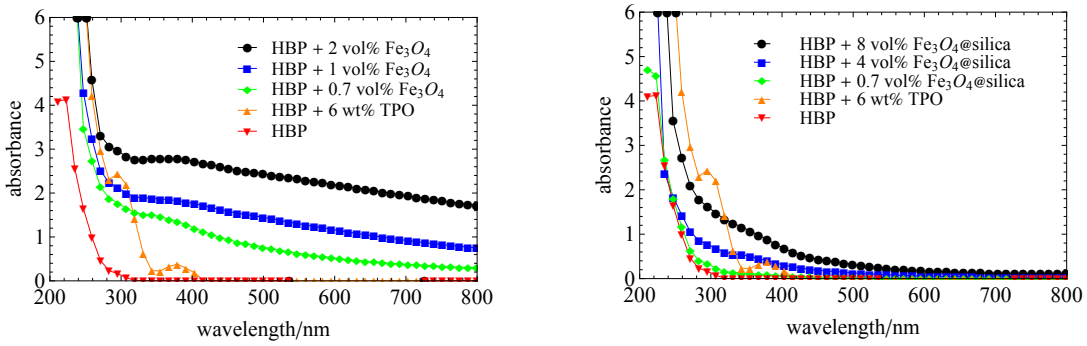

(a) (b)

The efficiency of the radical photoinitiator can be described by two quantum yields: the *quantum yields of initiation*, which represents the number of starting polymer chains per photons absorbed, and the *quantum yields of polymerization*, which is the number of monomer units polymerized per photons absorbed. Therefore, it is clear that the competition in absorption with the inorganic filler implies a decrease of the photons absorbed by the photoinitiator. This can lead to a decrease of quantum yields and therefore to a lower photopolymerization rate and acrylic double bond conversion.

In order to add a higher NPs content in the photocurable formulation, Fe_3O_4@SiO_2 NPs were synthesized. When the core-shell NPs are dispersed into the acrylic resin a good reactivity is preserved up to a particle content of 12 vol%. When 4 vol% of Fe_3O_4@SiO_2 NPs are dispersed into the acrylic resin, the final conversion decreased from 93% to 88%. Adding 8 vol% of the filler, the final acrylic double bond conversion underwent a minor drop to 84% with just a slight decrease of the slope of the conversion curve with respect to the pristine HBP. Compared to the formulations containing bare magnetite particles, the employment of core-shell structures allowed a nearly 10-fold increase in filler volume fraction.

This behavior is in agreement with the UV-Vis spectra (Fig. 7), which show a lower competitive absorption in the UV-region by the core-shell particles in comparison to the bare Fe_3O_4 NPs, therefore assuring a higher photo-efficiency in the same irradiation conditions and preserving satisfactory polymerization rate and final conversion.

The much faster and complete curing process that takes place when core-shell nanostructures are employed can be attributed to the optical properties of the filler.

A certain contribution to the improved photocurability of the system containing silica-coated nanoparticles comes from different light scattering behaviors between bare and core-shell nanoparticles. The loss of light passing thorugh a composite due to scattering can be evaluated by Equation 3 [23]

$$\frac{I}{I_0} = e^{-\left[\frac{32\phi_p x \pi^4 r^3 n_m^4}{\lambda^4}\left|\frac{\left(\frac{np}{nm}\right)^2-1}{\left(\frac{np}{nm}\right)^2+2}\right|^2\right]} \quad (3)$$

where I is the intensity of the transmitted light, I_0 the intensity of the incident light, r is the radius of the particles having refractive index n_p and dispersed in a matrix with refractive index n_m, ϕ_p is the particles volume fraction, λ the wavelength of light and x the optical path length. From Equation 3 it can be seen that when the refractive index of the particles matches that of the dispersing matrix, the loss of light due to scattering can be neglected and the light intensity available for the photoinitiator is maximized. The refractive indexes of silica, of magnetite and of HBP were taken from literature with values of 1.46 [13], 2.3 [24] and 1.47 (technical data), respectively, and the refractive index of the core-shell particles (≈1.49) was calculated as the average value of the refractive indices of the core and the shell through Equation 4 [25]

$$n_{composite} = \sum_i n_i^2 V_i \qquad (4)$$

where n_i and V_i are the refractive index and volume fraction of the individual components, respectively. As can be seen, the condensation of a silica shell around magnetite cores generates fillers with a refractive index almost matching that of the matrix, allowing to increase the filler volume fraction ϕ_p towards values which could have not been reached employing higher refractive index particles (e.g. magnetite NPs).

The same reasoning can be applied in order to explain the improved light transmittance of the systems containing Fe_3O_4@SiO_2 NPs compared to those filled with bare Fe_3O_4 NPs. Indeed, the UV-Vis spectra show a complete transparency of the photocured formulation containing Fe_3O_4@SiO_2 NPs in the visible region, while the bare Fe_3O_4 NPs strongly decreased the transparency of the crosslinked film in the same spectral portion (see Figure 8).

Figure 8: UV-vis absorbances as a function of the filler volume fraction for the systems containing bare Fe_3O_4 NPs and core-shell Fe_3O_4@silica NPs recorded at 500 nm. The dashed and the solid are the corresponding experimental fittings.

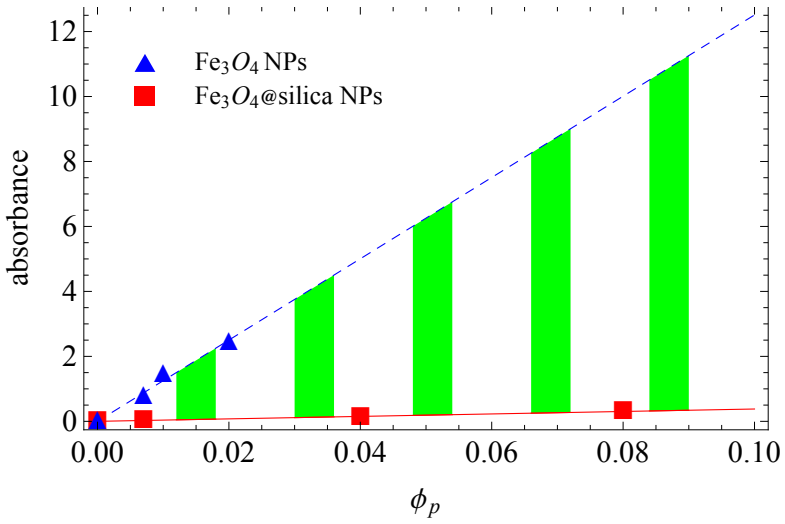

The choice to employ core-shell NPs has shown to be successful in order to increase the filler load while keeping a good photo-curability and film transparency.

3.4 UV-cured films

TEM micrographs of the UV-cured films containing 0.7 vol% of bare Fe_3O_4 NPs show a uniform dispersion of the magnetic filler in the polymeric matrix (Figure 9a). On the contrary, as soon as the concentration is raised to 2 vol% (Figure 9b) agglomeration between particles becomes important, hindering the transparency of the film and therefore precluding a good polymerization rate and final conversion.

Figure 9: Transmission electron micrographs of UV-cured films containing 0.7 vol% (a) and 2 vol% (b) of Fe_3O_4 NPs.

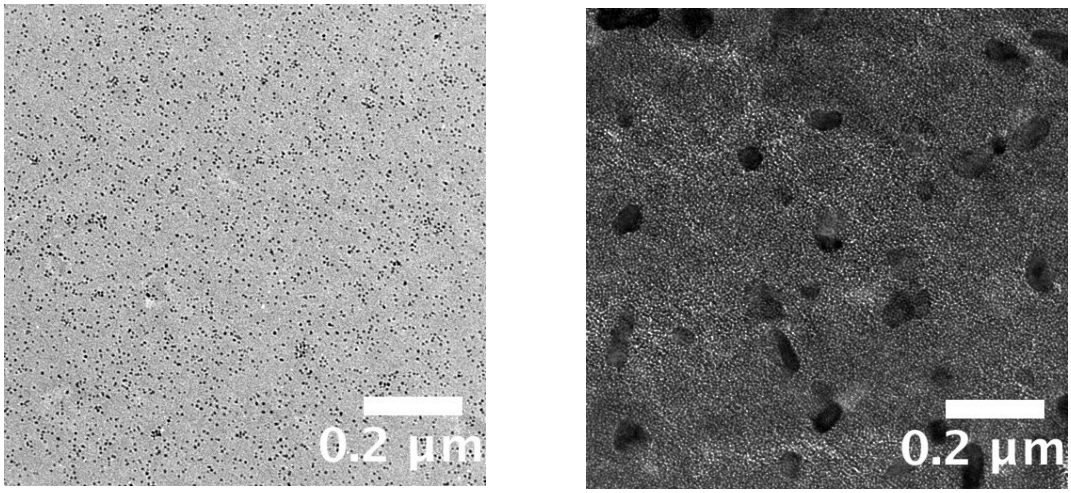

(a) (b)

Concerning the films containing core-shell nanoparticles, TEM micrographs show that at low particle volume fraction the dispersion (Figure 10a) is not as good as in the case of the film filled with bare magnetite particles, probably due to the fact that bigger agglomerates are formed during silica condensation. However, the number and dimension of the aggregates don't increase when higher loadings are reached and a

quite constant dispersion is maintained (Figure 10b-c). This effect can be explained by recalling that the Van der Walls force between nanoparticles is linearly dependent on their Hamaker constant. The Hamaker constant of silica being significantly lower than that of magnetite [26,27], the attractive force exerted by magnetite particles between one another is, for the same interparticle distance, higher than that generated between silica-coated particles.

Figure 10: Transmission electron micrographs of UV-cured films containing 0.7 vol% (a), 4 vol% (b) and 8 vol% (c) of Fe_3O_4@silica NPs.

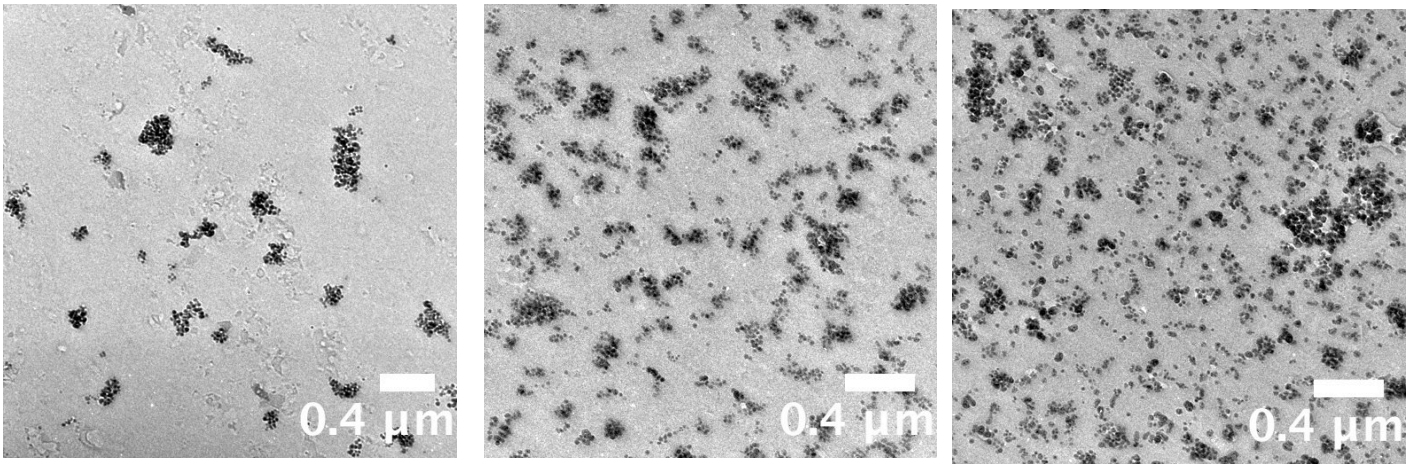

(a) *(b)* *(c)*

A thermo gravimetric analysis (TGA) (Figure 11) of the different formulations prior to UV-curing was performed in order to establish their effective filler content. Starting from this analysis and considering the morphology of the nanoparticles as evidenced by TEM, it was possible to estimate a comparable amount of iron oxide between the two systems containing 8 vol% of Fe_3O_4@SiO_2 NPs and 0.7 vol% of

bare Fe_3O_4 NPs. For this reason, only the magnetic properties of the cured films containing the above-mentioned quantities of nanofiller were evaluated.

Figure 11: TGA curves of HBP resin filled with 0.7 vol% Fe_3O_4 NPs and 8 vol% Fe_3O_4@silica NPs.

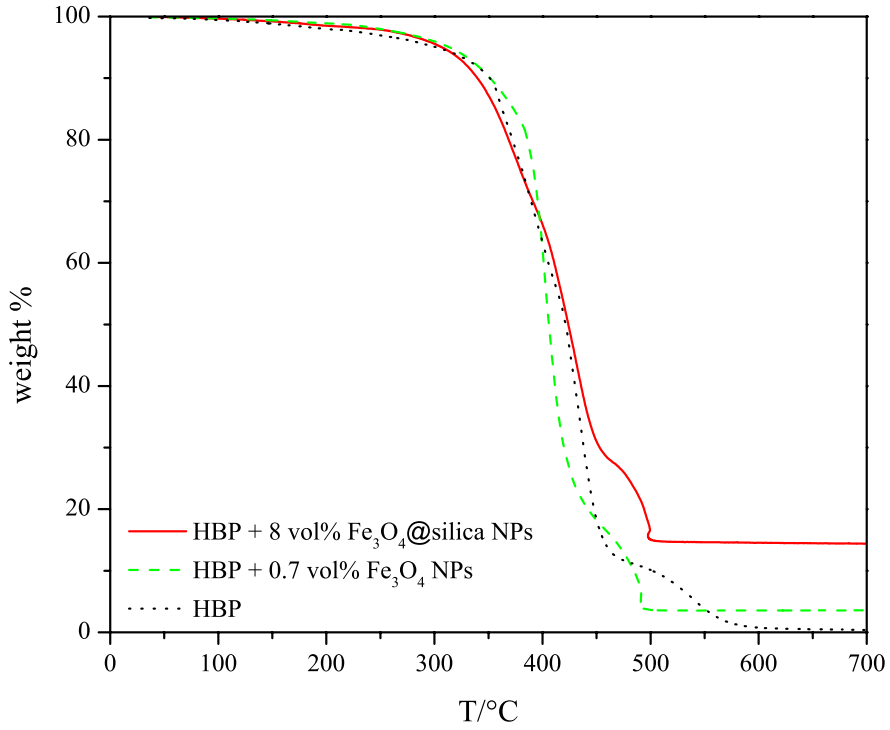

The room temperature magnetization curves of these two nanocomposites are reported in Fig. 12 (left panel). The host polymer only contributes a weak diamagnetic signal to the total curve, as observed comparing the magnitude of the magnetic response of both loaded films (black/red symbols) with the one of an unloaded film (green symbols); the small diamagnetic signal has been subtracted from the data reported in Fig. 12 for both nanocomposites. The magnetic response of the film containing core-shell NPs is comparable with the one of the material containing bare NPs, as expected on the basis of the similar iron oxide content in the two films; in addiction, the two curves have exactly the same shape and behavior, as checked by plotting the normalized magnetization $M/(H)/M_{15kOe}$ (right panel of Fig. 12). This

means that the silica shell has basically no influence on the overall magnetic response of our NPs. Actually, the magnitude of the magnetic response in the film containing core-shell NPOs is slightly lower than in the other film. This can be explained either by invoking a role of the silca-magnetite interface, where spin disorder at the surface of the magnetite core can be enhanced by the surrounding silica shell, or by considering that the individual magnetic moments of different magnetite NPs within the same silica shell can be antiferromagnetically coupled by dipolar interaction [28], decreasing the total apparent moment per core-shell nanoparticle. It is not possible to discard either model on the basis of a room temperature measurement alone; performing magnetic measurements down to low temperatures and up to larger fields will possibly help selecting the most accurate picture.

Figure 12: (left panel) room temperature magnetization curves of UV cured films containing bare and core-shell magnetite NPs; the magnetic response of the unloaded polymer is reported for comparison; (right panel) perfect superposition of normalized magnetization curves ($M(H)/M_{15kOe}$) in the magnetic nanocomposites.

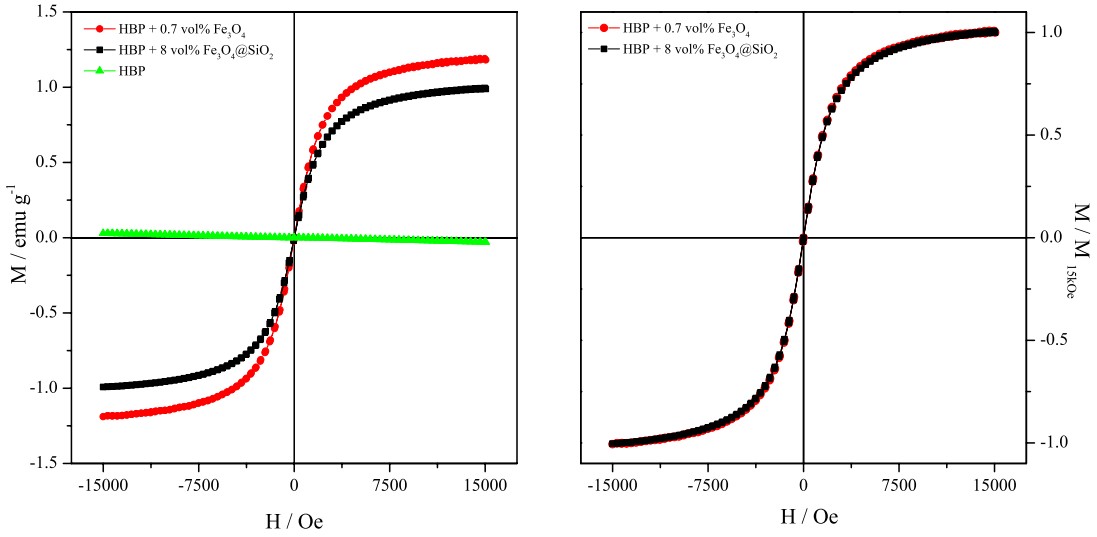

Magnetic measurements undoubtedly point out that the formulation containing 0.7 vol% of bare magnetite NPs have a similar magnetic behavior to that filled with 8 vol% of core-shell nanoparticles. However, the condensation of a silica shell and the attainment of such high filler loadings gains credit by recalling that many of the most important mechanical properties of composites, such as Young's modulus and Vickers hardness, rely upon the volume fractions of their reinforcing elements. Moreover, the presence of the silica shell is not only beneficial for the light accessibility of the photoinitiator, but it is also believed to be useful in order to add functionalities to the system. The ease with which silica can be functionalized could be exploited for many purposes. For example, an appropriate functionalization of the silica shell with sterically hindering or electrostatically charged groups could further improve the dispersion of the filler allowing to reach even higher particle volume fractions without facing the aggregation problem. Moreover, the magnetic response of the nanofillers could be exploited in order to concentrate the nanoparticles in specific regions of the film through magnetophoresis processes and generate materials with a continuous gradient of mechanical and magnetic properties.

4 Conclusions

The usage of Fe_3O_4@SiO_2 NPs for the synthesis of magnetic polymeric films through a fast and non-toxic photo-polymerization process has shown to be effective towards the inclusion of nearly 10-times higher particle volume fractions compared to formulations including bare magnetite particles (8 vol% compared to 0.7 vol%). The final conversion of formulations containing bare magnetite NPs dropped below 70% already at particle volume fractions as low as 1 vol%, whereas systems filled with core-shell NPs evidenced a remarkable 84% final conversion even at a filler content

of 8 vol%. At the same time, transparency of the UV-cured films in the visible region of the spectrum was highly improved in the case of the systems containing core-shell structures. Magnetic measurements pointed out that the system containing 8 vol% of core-shell particles had a similar magnetic behavior of that containing 0.7 vol% of bare magnetite nanoparticles (magnetization at 15000 *Oe* around 1 emu per gram of nanocomposite) indicating that the silica shell has little effect on the magnetic properties of magnetite cores, even if each shell typically hosts more than one magnetic core. As a matter of fact, core-shell magnetic nanofillers give rise to a much wider range of applications compared to bare nanoparticles without renouncing their magnetic properties. In particular, differential diffusion of core-shell nanoparticles sustained by magnetic field could be exploited to fabricate tailorable magnetic nanocomposites characterized by controlled composition gradients for prospective applications in medicine and ICTs.

Acknowledgement

The authors acknowledge the Swiss National Science Foundation (project 200020_144396) for financial support. Sincere acknowledgements also to Dr. Kurt Schenk (ISIC-EPFL) for the crystallographic characterization and to Gabriele Barrera, (University of Torino) for valuable help during magnetic measurements.

References

[1] S. Li, M. M. Lin, M. S. Toprak, D. K. Kim, M. Muhammed, *Nano Rev.* **2010**, *1*, 1-19.

[2] H. A. Patel, R. S. Somani,H. C. Bajaj, R. V. Jasra, *Bull. Mater. Sci.* **2006**, *29*(2), 133-145.

[3] T. Wen, K. M. Krishnan, *J. Phys. D: Appl. Phys.* **2011**, *44*, 1-24.

[4] M. González Lazo, R. Teuscher, Y. Leterrier, J.-A. E. Månson, C. Calderone, A. Hessler-Wyser, P. Couty, Y. Ziegler, D. Fischer, *Sol. Energ. Mat. Sol. C.* **2012**, *103*, 147-156.

[5] M. Sangermano, E. Amerio, P. Epicoco, A. Priola, G. Rizza, G. Malucelli, *Macromol. Mater. Eng.* **2007**, *292*, 634-640.

[6] M. Suter, O. Ergeneman, J. Zürcher, S. Schmid, A. Camenzind, B. J. Nelson, C. Hierold, *J. Micromech. Microeng.* **2011**, *21*, 1-8.

[7] D. K. Yi, S. S. Lee, J. Y. Ying, *Chem. Mater.* **2006**, *18*(10), 2459-2461.

[8] A. M. Schmidt, *Macromol. Rapid Comm.* **2006**, *27*(14), 1168-1172.

[9] J. Gass, P. Poddar, J. Almand, S. Srinath, H. Srikanth, *Adv. Funct. Mater.* **2006**, *16*(1), 71-75.

[10] C. Decker, *Polym. Int.* **1998**, *45*(2), 133–141.

[11] G. C. Xu, A. Y. Li, L. D. Zhang, G. S. Wu, X. Y.Yuan, T. Xie, *J. Appl. Polym. Sci.* **2003**, *90*(3), 837–840.

[12] M. Sangermano, B. Voit, F. Sordo, K. J. Eichhorn, G. Rizza, *Polymer* **2008**, *49*(8), 2018-2022.

[13] V. Geiser, Y. Leterrier, J.-A. E. Månson, *J. Appl. Polym. Sci.* **2009**, *114*(3), 1954–1963.

[14] V. Geiser, Y. Leterrier, J.-A. E. Månson, *Macromolecules* **2010**, *43*(18), 7705-7712.

[15] R. Jahn, T. Jung, *Prog. Org. Coat.* **2001**, *43*, 50-55.

[16] Z. Xu, C. Shen, Y. Hou, H. Gao, S. Sun, *Chem. Mater.* **2009**, *21*(9), 1778-1780.

[17] S. Tasic, B. Bozic, B. Dunjic, *Prog. Org. Coat.* **2004**, *51*(4), 320-327.

[18] P. Scherrer, *Nachr. Ges. Wiss. Göttingen* **1918**, *26*, 98-100.

[19] J. D. Hanawalt, *Anal. Chem.* **1938**, *10*, 475.

[20] B. D. Cullity, C. D. Graham, in *Introduction to Magnetic Materials, 2nd ed.*, John Wiley & Sons, Inc., Hoboken, New Jersey **2009**.

[21] P. Dutta, S. Pal, M. S. Seehra, N. Shah, G. P. Huffmann, *J. Appl. Phys.* **2009**, 105(7), 07B501 - 07B501-3.

[22] M. Knobel, W. C. Nunes, L. M. Socolovsky, E. De Biasi, J. M. Vargas, J. C. Denardin, *J. Nanosci. Nanotechnol.* **2008**, *8*(6), 2836-2857.

[23] W. Caseri, *Chem. Eng. Comm.* **2009**, *196*(5), 549-572.

[24] X. Q. Xu, H. Shen, J.R. Xu, M.Q. Xie, X.J. Li, *Appl. Surf. Sci.* **2006**, *253*(4), 2158-2164.

[25] Y.-Q. Li, S.-Y. Fu, Y. Yang, Y.-W. Mai, *Chem. Mater.* **2008**, *20*(8), 2637-2643.

[26] L. Bergström, *Adv. Colloid. Interfac.* **1997**, *70*, 125-169.

[27] B. Faure, G. Salazar-Alvarez, L. Bergström, *Langmuir* **2011**, *27*(14), 8659-8664.

[28] C. Xu, Y. Q. Ma, P. M. Hui, *J. Appl. Phys.* **2005**, *98*(8), 084303 - 084303-8.